

# Dynamics of transient cavities

V. DUCLAUX<sup>1</sup>, F. CAILLÉ<sup>1</sup>, C. DUEZ<sup>2</sup>, C. YBERT<sup>2</sup>,  
L. BOCQUET<sup>2</sup> AND C. CLANET<sup>1</sup>

<sup>1</sup>IRPHE, UMR 6594, 49 rue F. Joliot-Curie, BP 146, 13384 Marseille, France

<sup>2</sup>Laboratoire PMCN, UMR CNRS 5586, Université Lyon I, 69622 Villeurbanne, France

(Received 1 December 2005 and in revised form 10 May 2007)

We study the collapse of a transient cavity of air in water created by the impact of a solid body. Experimentally, we characterize the dynamics of the cavity from its creation ( $t = 0$ ) until it collapses ( $t = \tau$ ) in the limit where inertia dominates viscous and capillary effects. Theoretically, we find in this regime an approximate analytical solution which describes the time evolution of the shape of the cavity. This theoretical solution predicts the existence of two different types of cavities that we also observe experimentally.

---

## 1. Introduction

What happens when a solid body impacts on water?

A few decades ago, this question was of interest for seaplane engineers (von Kármán 1929; Wagner 1932), naval architects (Cointem 1989; Fridman 1998), torpedo designers (May 1952; Richardson 1948) and physicists interested in fast transient phenomena (Worthington 1908). Lately, it has become of interest for mechanicians interested in the Basilic lizard motion (Glasheen & McMahon 1996*b*) and physicists working on granular flows (Thoroddsen & Shen 2001; Lohse *et al.* 2004).

This question belongs to the general subject of *water entry problems* which is mainly composed of two different kinds of studies: the initial stages of contact (Korobkin & Pukhnachov 1988; Howison, Ockendon & Wilson 1991) and the creation of the associated cavity (Birkhoff & Zarantonello 1957). The present article belongs to this second class of studies.

A typical impact is presented in figure 1. This chronophotography presents the evolution of the cavity during the first 140 ms after the impact of a glass sphere covered with soot (hydrophobic surface). The radius is  $R_0 = 12$  mm and the velocity  $U = 2.1$  m s<sup>-1</sup> ( $Fr = 39$ ). The creation of the cavity extends from image 1 to image 8 where it pinches. We denote the depth of the cavity at pinching  $H$  and the position of the neck  $H_p$ . The diameter of the hole at the surface ( $z = 0$ ) is  $2R$ . If  $t = 0$  stands for the time at which the sphere touches the interface, the time of pinching is defined as  $t = \tau$ .

After the pinching (images 9 to 16) both cavities ( $0 < z < H_p$  and  $H_p < z < H$ ) retract, one towards the surface ( $0 < z < H_p$ ) and the other towards the sphere ( $H_p < z < H$ ). In this article, we focus on the dynamics of the cavity from creation to pinching (images 1 to 8).

If  $\sigma$  stands for the surface tension,  $\sigma R_0^2$  is the order of magnitude of the energy required to perturb the surface over the scale  $R_0$ . Using  $\rho$  for the liquid density, one expects the cavity to be created when the kinetic energy of the impact  $\sim \rho R_0^3 U^2$

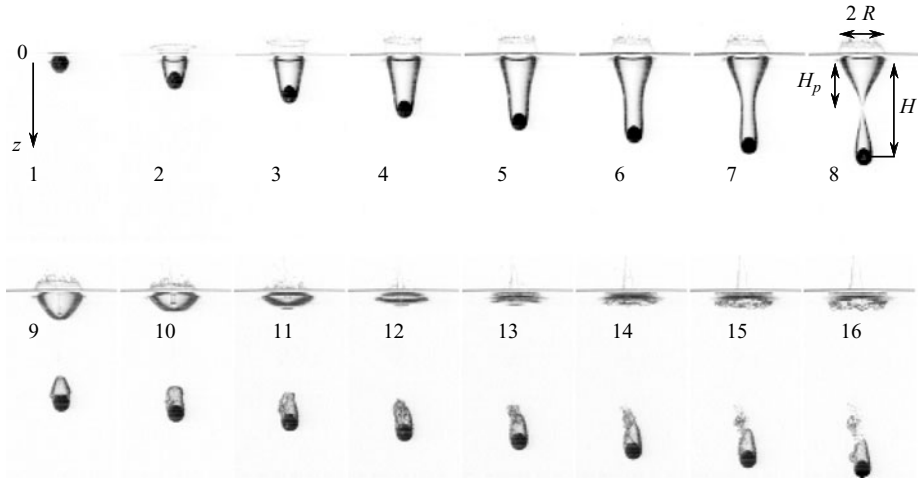


FIGURE 1. Chronophotography of the impact of a sphere ( $R_0 = 12$  mm) at  $U = 2.1$  m/s ( $Fr = 39$ ). The time step between images is  $\Delta t = 9.3$  ms. The sphere is coated with carbon soot.

is much larger than this surface energy. The study is thus conducted in the limit of high Weber number:  $We \equiv \rho U^2 R_0 / \sigma \gg 1$ . This is true as long as the kinetic energy is not completely dissipated at the impact through viscosity  $\mu U R_0^2$ , where  $\mu$  is the dynamic liquid viscosity. This second condition implies that the Reynolds number  $Re \equiv \rho U R_0 / \mu$  is much larger than unity. In the example presented in figure 1, we find  $We \approx 750$  and  $Re \approx 25000$ .

In this parameter range ( $We \gg 1$ ,  $Re \gg 1$ ), Glasheen & McMahon (1996a) summarize the experimental results obtained during the impact of a disk (radius  $R_0$ ) in water as:

the depth of the cavity scales as  $H/R_0 \approx 2.297 U / \sqrt{g R_0}$ ;

the time for pinching scales as  $\tau \approx 2.285 \sqrt{R_0/g}$  and is reported to be ‘nearly independent of the velocity’.

These experimental results are obtained for ‘low Froude numbers’:  $1 \leq U^2/g R_0 \leq 80$ . No theoretical model is proposed to account for these laws.

On the other hand, considering the impact in soft sand, Lohse *et al.* (2004) propose an hydrodynamic approach to describe the cavity created by the impact of a solid sphere in sand and propose the following scaling behaviour for its depth:  $H/R_0 \sim Fr^{1/3}$ .

In the present article, we first present experimental results on cavities created in water by spheres and cylinders. A model is then proposed to account for the experimental observations and to understand the origin of the two different laws proposed by Glasheen & McMahon (1996a) & Lohse *et al.* (2004).

## 2. Experimental set-up

### 2.1. Synopsis of the experiment

A sketch of the experiment is presented in figure 2(a): the solid sphere (or cylinder) is initially fixed at a height  $H_0$  above the water surface and is maintained at rest using a suction disk (holding device). Suddenly, the suction is released and the sphere (or cylinder) accelerates under its own weight towards the water and impacts at  $t=0$  with a velocity close to  $U \approx \sqrt{2gH_0}$ . The velocity is precisely measured at

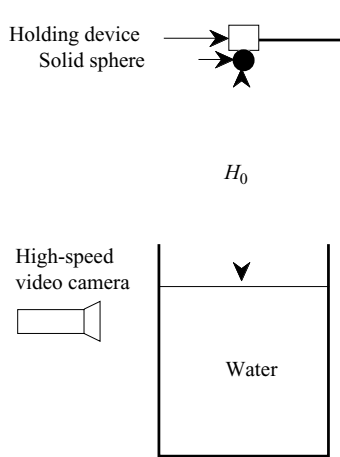


FIGURE 2. Sketch of the experimental set-up.

Sphere	$R_0$ (mm)	$M$ (g)	Cylinder	$R_0$ (mm)	$L$ (g)	$M$ (g)
S1	6	7	C1	6.1	100	21.4
S2	7.8	4.7	C2	10.1	200	31.2
S3	12	18	C3	20.1	400	243.2
S4	20	32				

TABLE 1. Geometrical characteristics of spheres and cylinders.

$H_0$ (m)	$R_0$ (mm)	$Re \equiv \frac{UR_0}{\nu}$	$We \equiv \frac{\rho U^2 R_0}{\sigma}$	$Fr \equiv \frac{U^2}{gR_0}$
0.1	6	$8.4 \times 10^3$	168	33
1	6	$2.6 \times 10^4$	1680	330
0.1	20	$2.8 \times 10^4$	560	10
1	20	$8.8 \times 10^4$	5605	100

TABLE 2. Orders of magnitude of the characteristic non-dimensional numbers, Reynolds, Weber and Froude, obtained for two different spheres released from two different heights.

the impact using a high-speed video camera, which also records the whole impact sequence.

## 2.2. Characteristics of the spheres and cylinders

The geometrical characteristics of the spheres and cylinders are presented in table 1. Their radius  $R_0$  ranges from 6 mm to 20 mm. Their impact in water (density  $\rho \approx 10^3 \text{ kg m}^{-3}$ , surface tension  $\sigma \approx 0.07 \text{ kg s}^{-2}$ , kinematic viscosity  $\nu \approx 10^{-6} \text{ m}^2 \text{ s}^{-1}$ ) is characterized by three non-dimensional numbers: Reynolds  $Re \equiv UR_0/\nu$ , Weber  $We \equiv \rho U^2 R_0/\sigma$  and Froude  $Fr \equiv U^2/gR_0$ , respectively comparing inertia to viscous, capillary and gravitational forces. The range of variation of these numbers in our experiment is presented on table 2. We observe that the whole study is conducted in the limit of high Reynolds and Weber numbers and for ‘moderate’ Froude numbers.

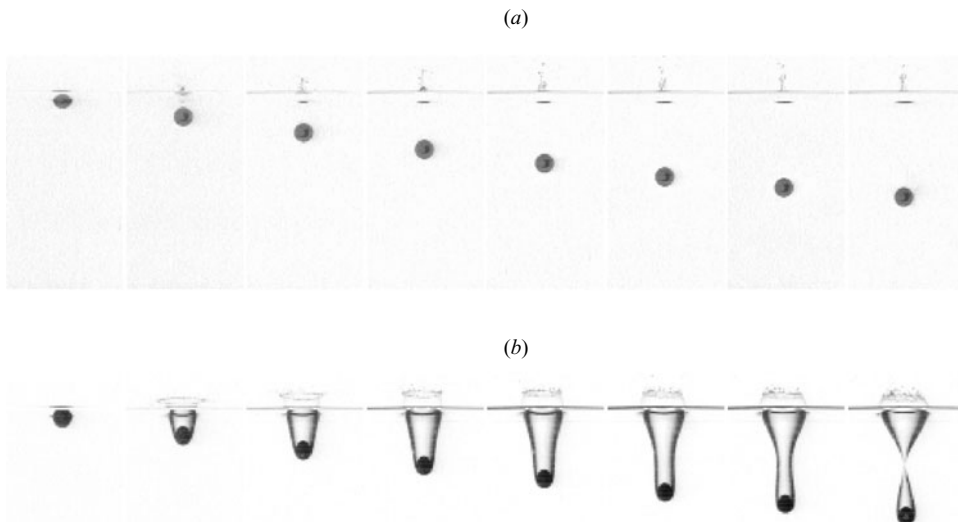


FIGURE 3. Chronophotography of the impact of (a) a smooth sphere of glass ( $R_0 = 12$  mm) and (b) the same sphere coated with soot, at  $U = 2.1 \text{ m s}^{-1}$  ( $Fr = 39$ ). The time step between images is  $\Delta t = 9.3$  ms in both sequences.

### 3. Experimental results

#### 3.1. Threshold of entrainment

In figure 3 we present the impact of a sphere ( $R_0 = 12$  mm) at the velocity  $U = 2.1 \text{ m s}^{-1}$  ( $Fr = 39$ ) that is either hydrophilic (clean glass surface in figure 3a), or hydrophobic (the same glass sphere coated with soot in figure 3b). We observe that the cavity shown in figure 1 only exists in the ‘hydrophobic’ case.

The same experiment conducted with a higher impact velocity  $U = 8 \text{ m s}^{-1}$  ( $Fr = 543$ ) is presented in figure 4. Here, we do not observe any significant difference between the cavity created by the hydrophilic sphere (figure 4a) and the one created by the hydrophobic sphere (figure 4b).

From both experiments, we can conclude that the cavity presented in figure 1 only exists above a threshold velocity, the value of which depends on the surface state. Above this velocity, no significant difference can be observed on the shape of the cavity created.

The hydrophilic (or hydrophobic) property of the surface results from its roughness and wetting properties (de Gennes, Brochard & Quéré 2004). Here, we simply note that the hydrophobicity of the surface plays a role in the threshold of entrainment, without entering into the detail of the specific role of wetting and roughness. This specific study is reported in Duez *et al.* (2007) and Eggers (2007).

To qualitatively understand the influence of the surface hydrophobicity on the threshold of entrainment, one must focus on the dynamics of the liquid film which develops around the sphere during the first instants of the contact between the sphere and the interface. This is done in figure 5, where we show that the liquid film (the position of which is indicated with arrows) moves along the surface as the sphere crosses the interface. In the hydrophilic case (figure 5a) the film reaches the ‘north pole’ in a time  $\tau_{film}$  smaller than the time  $2R_0/U$  needed for the sphere to cross the interface. In the second sequence (figure 5b) the liquid film created at the impact does

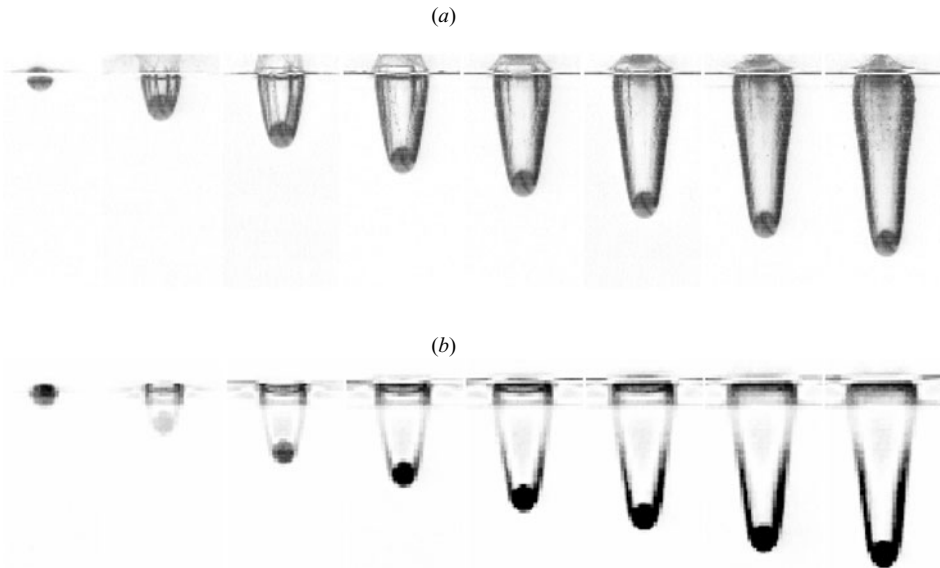


FIGURE 4. Chronophotography of the impact of (a) a smooth sphere of glass ( $R = 12$  mm) and (b) the same sphere coated with carbon soot at  $U = 8$  m s $^{-1}$  ( $Fr = 543$ ). The time step between images is  $\Delta t = 3.65$  ms.

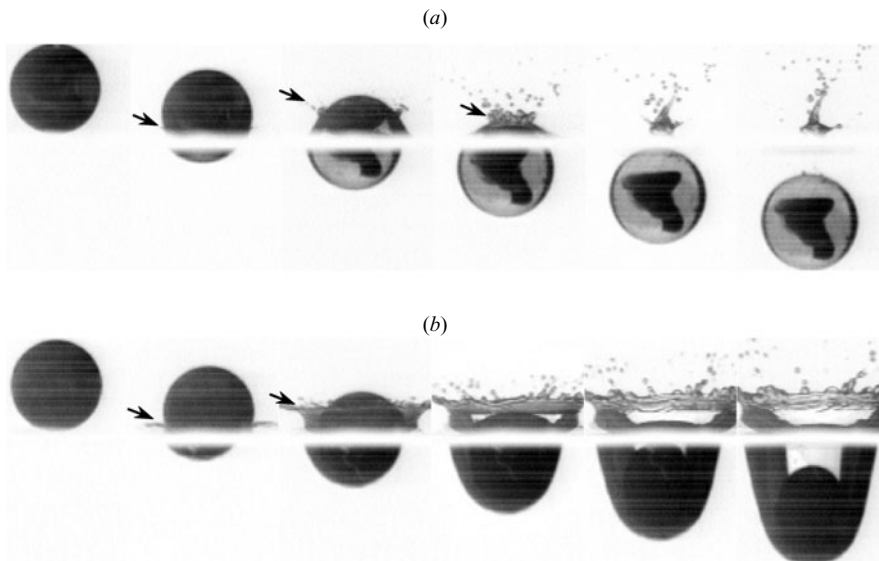


FIGURE 5. Chronophotography of the impact of (a) a hydrophilic sphere of glass ( $R_0 = 7.8$  mm) and (b) the same sphere coated with carbon soot (hydrophobic) at  $U = 1.34$  m s $^{-1}$  ( $Fr = 23$ ). The time step between images is  $\Delta t = 3.3$  ms. The arrows indicate the position of the liquid film over the sphere.

not converge towards the ‘north pole’ and the hydrophobic sphere (the same glass sphere but coated with soot) entrains air and creates the cavity.

The influence of the surface roughness on the creation of the cavity has been known since the pioneering work of Worthington & Cole (1900) as can be seen on figure 6.

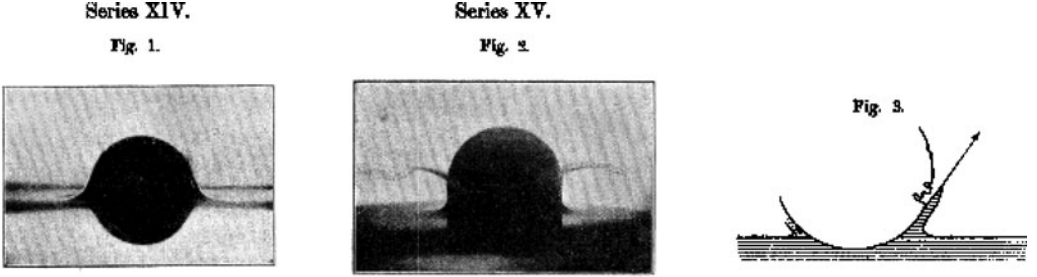


FIGURE 6. Figures extracted from Worthington & Cole (1900): (a) impact in water of a smooth sphere (b) impact at the same conditions of a rough sphere (c) proposed mechanism for the influence of the roughness.

The film dynamics observed for smooth sphere impact is presented in figure 6(a), that of the rough sphere in figure 6(b) and a proposed scenario to understand the influence of the roughness is sketched in figure 6(c). That landmark study is more complete than the present one on the transition from smooth to rough since it discusses the influence of the liquid viscosity, surface tension, air pressure, and even sphere temperature. Here, we just want to underline that the origin of the transition lies in the dynamics of the thin film which develops in the very first instants of the impact. The study of the initial stage of contact belongs to the first kind of studies mentioned above, dedicated to water entry (Oliver 2002). The threshold problem is outside the scope of the present work and in the remaining part of the article, we focus on the dynamics of the transient cavities and only consider cases where the impact velocity is above the critical velocity of entrainment.

### 3.2. Influence on the cavity of the impact velocity $U$ for a fixed radius $R_0$

The influence of the impact velocity for a fixed radius ( $R_0 = 7.8$  mm) is presented in figure 7 for three different velocities ( $U = 1.3, 2.4$  and  $3.7$  m s<sup>-1</sup>). The time step between the images is constant for the three chronophotographies ( $\Delta t = 7.3$  ms) and the dashed lines indicate the constant velocity limits. The first observation is that the cavity is created with an almost constant velocity up to the pinching. There is however a weak deceleration of the sphere associated to the liquid entrainment which can be observed through the deviation from the dashed line.

The second striking observation from figure 7 is that the pinching of the cavities occurs at the same time for the three different velocities  $\tau \approx 52$  ms.

Taking the relative cavity depth as  $H/R_0$ , we measured  $H/R_0 \approx 7.5$  for  $U = 1.3$  m s<sup>-1</sup>,  $H/R_0 \approx 13$  for  $U = 2.4$  m s<sup>-1</sup> and  $H/R_0 \approx 17$  for  $U = 3.7$  m s<sup>-1</sup>. The cavity depth seems to increase linearly with the velocity.

Taking the relative size of the hole at the surface as  $R/R_0$ , we measure  $R/R_0 \approx 1.9$  for  $U = 1.3$  m s<sup>-1</sup>,  $R/R_0 \approx 3$  for  $U = 2.4$  m s<sup>-1</sup> and  $R/R_0 \approx 3.3$  for  $U = 3.7$  m s<sup>-1</sup>. The size of the hole increases with the velocity but less than linearly.

Regarding the neck location, the three chronophotographies indicate that  $H_p$  is of the order of  $H/2$ .

### 3.3. Influence on the cavity of the radius $R_0$ , for a fixed velocity $U$

The influence of the radius, for a fixed velocity  $U = 1.3$  m s<sup>-1</sup>, is presented in figure 8. The time to pinching is  $\tau \approx 52$  ms for  $R_0 = 7.8$  mm and increases with  $R_0$  to reach  $\tau \approx 66$  ms for  $R_0 = 12$  mm.

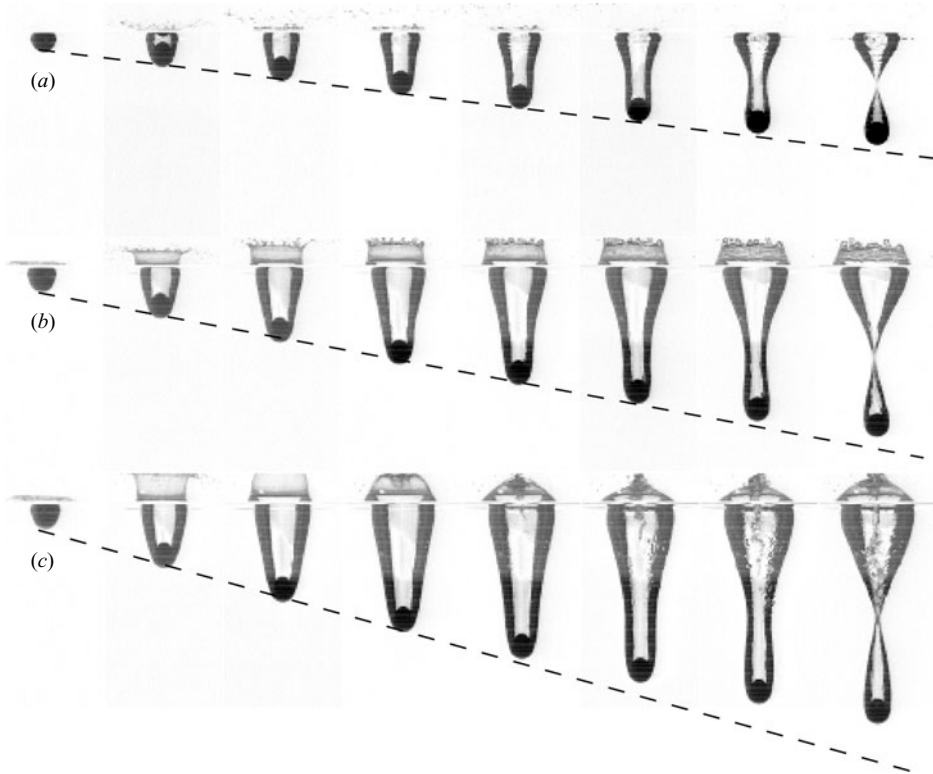


FIGURE 7. Influence of the impact velocity  $U$  for a fixed radius  $R_0 = 7.8$  mm. The time step between the images is constant for the three chronophotographies  $\Delta t = 7.3$  ms: (a)  $U = 1.3$  m s $^{-1}$ ,  $Fr = 22$ ; (b)  $U = 2.4$  m/s $^{-1}$ ,  $Fr = 80$ ; (c)  $U = 3.7$  m s $^{-1}$ ,  $Fr = 188$ . The dashed lines indicate the constant velocity limits.

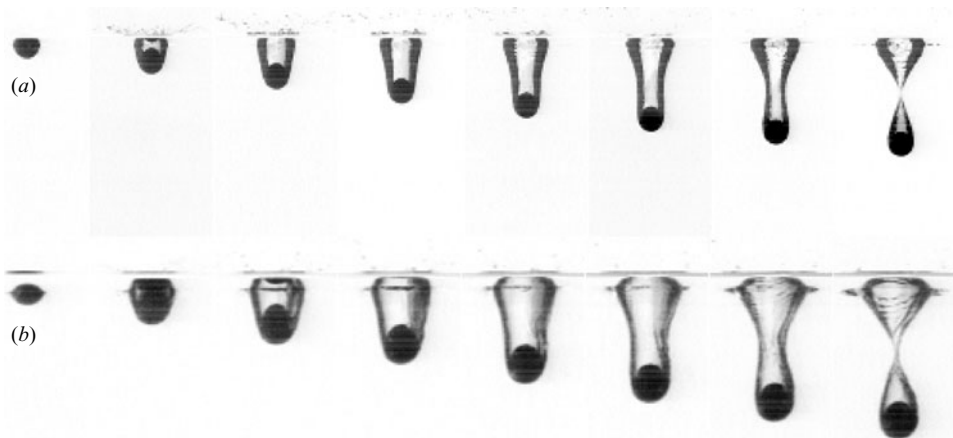


FIGURE 8. Influence of the radius  $R_0$  for a fixed impact velocity  $U = 1.3$  m s $^{-1}$ . (a)  $R_0 = 7.8$  mm,  $Fr = 22$ . The time step between images is  $\Delta t = 7.3$  ms. (b)  $R_0 = 12$  mm,  $Fr = 14.3$ . The time step between images is  $\Delta t = 9.3$  ms.

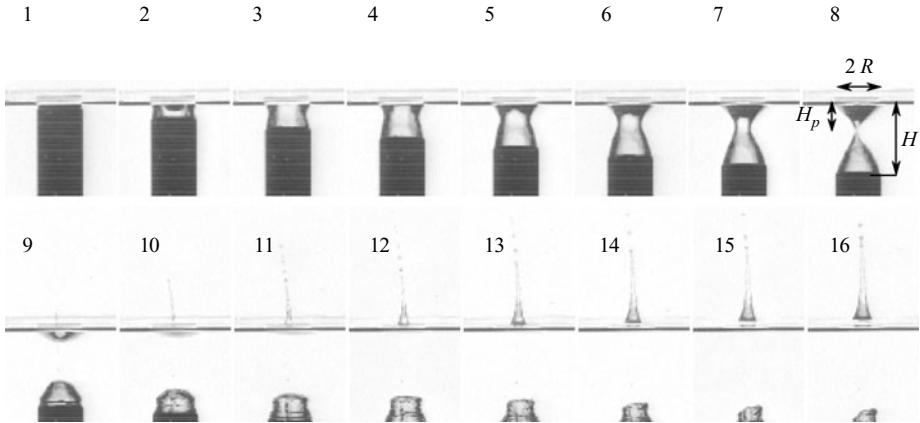


FIGURE 9. Impact of a cylinder ( $R_0 = 10$  mm) at  $U = 1.06$  m s $^{-1}$  ( $Fr = 11$ ). The time step between images is  $\Delta t = 4$  ms.

The relative depth  $H/R_0$  decreases with  $R_0$ : we measure  $H/R_0 \approx 7.5$  for  $R_0 = 7.8$  mm and  $H/R_0 \approx 6.7$  for  $R_0 = 12$  mm.

Finally, the relative crater size  $R/R_0$  remains almost constant: we measure  $R/R_0 \approx 1.9$  for both cases.

### 3.4. Impact of cylinders

An example of impact with cylinders is presented in figure 9 where a cylinder ( $R_0 = 10$  mm) impacts at  $U = 1.06$  m s $^{-1}$  ( $Fr = 11$ ). When the back of the cylinder crosses the interface, it entrains air and forms a cavity which pinches in a characteristic time  $\tau \approx 28$  ms.

Qualitatively, the features of this cavity are similar to those of a sphere and shown in figure 1. Looking more carefully at the pictures, one may however see at least three differences:

- (i) the radial extent of this cavity never exceeds the size of the cylinder;
  - (ii) the crater at the surface scales with the diameter of the cylinder ( $R/R_0 \approx 1$ ) and does not grow in time;
  - (iii) the position of the neck is not at  $H/2$  but closer to the interface ( $H_p/H \approx 0.35$ )
- We examine more quantitatively the differences between the cavities created by spheres and cylinders in § 5.

## 4. Model

### 4.1. The Besant (1859)–Rayleigh (1917) problem

The first problem we consider, in order to model the cavity collapse, is the classical Besant–Rayleigh problem (Besant 1859; Rayleigh 1917): “An infinite mass of homogeneous incompressible fluid acted upon by no forces is at rest, and a spherical portion of the fluid is suddenly annihilated; it is required to find the instantaneous alteration of pressure at any point of the mass, and the time in which the cavity will be filled up, the pressure at an infinite distance being supposed to remain constant”. Experimentally, this mind experiment can be approached using collapsing bubbles, as presented in figure 10 extracted from Batchelor (1967).

This classical Besant–Rayleigh problem is contained in textbooks and review articles (Brennen 1995; Brenner, Hilgenfeldt & Lohse 2002) and its resolution has



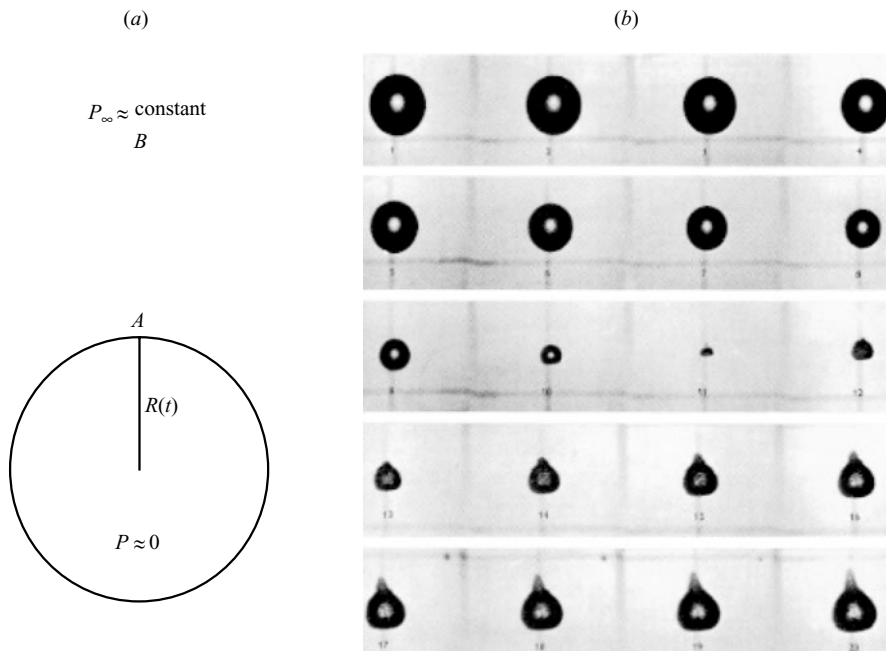


FIGURE 10. (a) Sketch of the Besant–Rayleigh problem. (b) Figure extracted from Batchelor’s (1967) textbook: Photographs of a collapsing cavity in a stationary vessel of water at intervals of  $2 \cdot 10^{-4}$  s. The cavity was formed by putting the water in tension for a brief period, with a minute bubble of gas released by electrolysis as the nucleus. During the period covered by the photographs the pressure difference  $p_0 - p_v$  was maintained at 0.051 atm. The mean radius of the cavity in the first photograph is 0.69 cm, and the minimum volume occurs between the 10th and 11th photographs. Photographs 11 to 20 show a rebound with characteristic non-spherical form. (Unpublished photographs by T. B. Benjamin and A. T. Ellis.)

been undertaken in more detail than the presentation below (Hilgenfeldt *et al.* 1998). The only purpose of the present treatment is to introduce a new analytical approach and check its validity on a classical problem. The method is then applied in §4.2 to analyse the cylindrical cavity limit for which no analytical solution is known.

In figure 10(b) the Reynolds number can be evaluated as  $Re \approx R^2/\tau \nu \approx 25\,000$ , where  $R \approx 0.69$  cm is the initial size of the cavity and  $\tau \approx 2$  ms is the time of collapse. In this high-Reynolds-number limit the motion of the liquid can be described by the Euler equation:

$$\frac{\partial \mathbf{u}}{\partial t} + \text{grad } \mathbf{u} \cdot \mathbf{u} = -\frac{1}{\rho} \text{grad } p. \quad (4.1)$$

Since the fluid is initially at rest, the motion is irrotational at all times and its velocity can be described through a potential  $\phi$ :  $\mathbf{u} = \text{grad } \phi$ . Equation (4.1) can be integrated in this limit and leads to the so-called generalized Bernoulli equation:

$$\left[ \frac{\partial \phi}{\partial t} + \frac{u^2}{2} + \frac{p}{\rho} \right]_A^B = 0 \quad (4.2)$$

where  $A$  and  $B$  stand for two points in the fluid. For the Besant–Rayleigh problem sketched in figure 10(a), point  $A$  is chosen behind the cavity surface ( $r_A = R(t)$ ) and point  $B$  in a region ‘far’ from the cavity where there is no motion. In this case,

equation (4.2) can be written:

$$\frac{\partial \phi}{\partial t} \Big|_A + \frac{u_A^2}{2} = \frac{p_\infty}{\rho}. \quad (4.3)$$

Here, we assume that the pressure  $p_\infty$  ‘far’ from the cavity is constant and large compared to the pressure inside the cavity. As usual, this momentum equation must be completed by the equation of mass conservation which reduces, with our assumptions of incompressible and potential flow, to  $\Delta \phi = 0$ . In this limit, and using the spherical symmetry of the problem, the velocity  $u$  at any point  $r > R$  can be deduced from the interface location  $R(t)$  and its velocity  $\dot{R}$  through the relation:

$$u = \left( \frac{R}{r} \right)^2 \dot{R}, \quad (4.4)$$

from which we find  $\phi(r, t) = -R(t)^2 \dot{R}/r$  and can deduce the equation for the cavity collapse:

$$R\ddot{R} + \frac{3}{2}\dot{R}^2 = -\frac{p_\infty}{\rho} \quad (4.5)$$

which must be integrated with the initial conditions  $R(t=0) = R_0$  and  $\dot{R}(t=0) = 0$ . Solving in  $\dot{R}$ , equation (4.5) can be integrated once as

$$\dot{R}^2 = \frac{2}{3} \frac{p_\infty}{\rho} \left[ \left( \frac{R_0}{R} \right)^3 - 1 \right] \quad (4.6)$$

from which we obtain the time of collapse  $\tau$ :

$$\tau = \int_0^{R_0} \frac{dR}{\sqrt{\frac{2}{3}(p_\infty/\rho) [(R_0/R)^3 - 1]}} = 0.914 \frac{R_0}{\sqrt{p_\infty/\rho}}. \quad (4.7)$$

The trajectory  $R(t)$  obtained through the integration  $R(t) = \int_0^t \dot{R} dt$  is compared by Batchelor (1967) to the experimental collapse presented on figure 10 and is found in fair agreement up to the minimal radius. The bouncing of the cavity which is observed on figure 10(b) after the minimal radius is related to the compression of the gas during the bubble collapse, an effect which is not accounted for in the present rough theory. If one now considers the singularity  $R \rightarrow 0$ , equation (4.6) shows that

$$R(t) \sim \left( \frac{2}{3} \frac{p_\infty}{\rho} R_0^3 \right)^{1/5} (\tau - t)^{2/5}. \quad (4.8)$$

### Summary

In this classical example, one obtains an exact solution for the velocity (4.6), but no analytical expression for the evolution  $R(t)$ . This evolution must be obtained through a numerical integration. There are cases, such as the cylindrical cavity, where such an analytical expression, even approximate, can be useful. This is the motivation for the method we develop now, the accuracy of which will be tested on the Besant–Rayleigh problem.

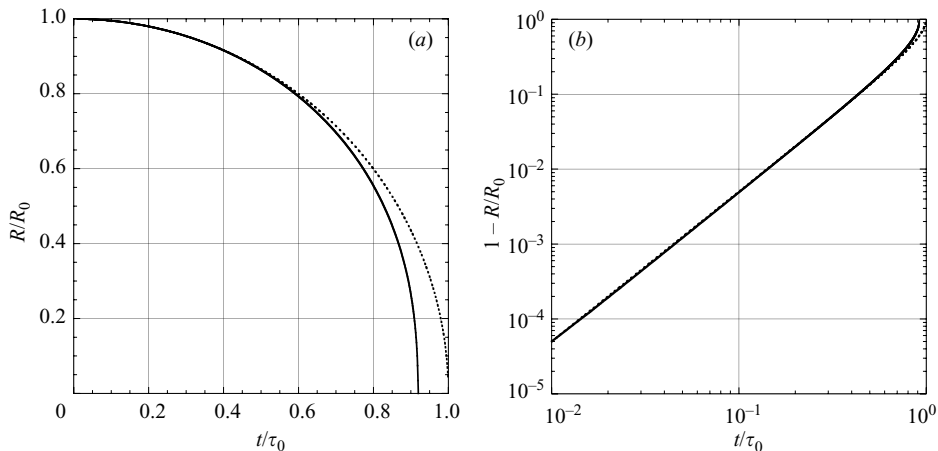


FIGURE 11. (a) Comparison between the exact solution of the Besant–Rayleigh problem (numerical integration of (4.6)) (solid line) and the approximate solution (4.11) (dashed line): (a)  $R/R_0(t/\tau_0)$  presented on a linear scale (b)  $1 - R/R_0(t/\tau_0)$  presented on a log-log scale.

#### Presentation of the approximate analytical method

Using the observation that  $\ddot{R}^2 \equiv d^2 R^2/dt^2 = 2(R\ddot{R} + \dot{R}^2)$ , one can re-write the equation for the cavity (4.5) as

$$\ddot{R}^2 + \dot{R}^2 = -\frac{2 p_\infty}{\rho}. \quad (4.9)$$

Since  $\dot{R}$  is null initially, the dynamics of the cavity is initially described by

$$\ddot{R}^2 \approx -\frac{2 p_\infty}{\rho}, \quad (4.10)$$

the solution of which is

$$R = R_0 \sqrt{1 - (t/\tau_0)^2} \quad (4.11)$$

with  $\tau_0 \equiv R_0/\sqrt{p_\infty/\rho}$ . This approximate analytical solution holds provided  $\dot{R}^2$  remains smaller than  $2p_\infty/\rho$ , that is provided  $(t/\tau_0)^2/[1 - (t/\tau_0)^2] \ll 2$ . This solution is thus expected to be valid at the beginning of the collapse and is expected to fail close to the singularity.

A comparison between the exact trajectory  $R(t)$  (obtained numerically through the integration of equation (4.6)) and the approximate solution (4.11) is presented in figure 11, with a linear scale in 11(a) and a log-log scale in 11(b). As expected, the behaviour of the approximation is good for small time and deviate from the exact solution for times larger than  $t/\tau_0 > 0.8$ . If one considers the time of collapse, the approximate solution gives  $t = \tau_0$  which is 9% above the exact value (equation (4.7)).

The limits of the approximate analytical solution are reached at the singularity: at the singularity, the approximate solution leads to

$$R(t) \sim \left( \frac{4R_0^2 p_\infty}{\rho} \right)^{1/4} \sqrt{\tau_0 - t} \quad (4.12)$$

which is different from the exact behaviour (4.8), the scaling in time being 1/2 instead of 2/5. From equation (4.9), it is seen that at the singularity, the second term  $\dot{R}^2$  diverges while the third term (the pressure) remains constant. This can only be

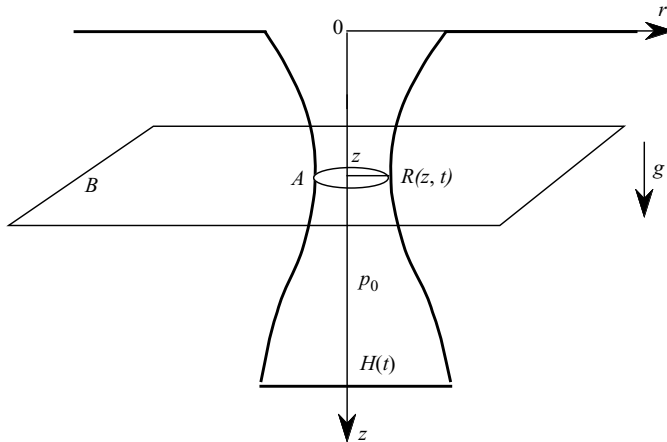


FIGURE 12. Conventions used to describe the dynamic of the cylindrical cavity.

achieved if the first two terms compensate, that is if  $\ddot{R}^2 + \dot{R}^2 = 0$ , or  $R \sim (\tau - t)^{2/5}$ . As already underlined, the approximate solution only holds as long as the second term remains small compared to the third one.

To conclude this section on the validity of the approximate equation (4.10) in describing the dynamics of the cavity collapse, we observe that most of the dynamics is captured except at the singularity.

#### 4.2. The cylindrical cavity problem

We now turn to the cylindrical cavity problem presented in figure 12: a solid body impinges vertically through the surface and creates an axisymmetric cavity which first expands radially prior to closure. The characteristics of the cavity have been discussed in §3 and we present here the modelling of the dynamics using the notation presented in figure 12.

Following the approach used to solve the Besant–Rayleigh problem, we first complete the generalized Bernoulli equation, taking gravity into account:

$$\left[ \frac{\partial \phi}{\partial t} + \frac{u^2}{2} + \frac{p}{\rho} - gz \right]_A^B = 0. \quad (4.13)$$

Choosing  $A$  in the liquid behind the interface and  $B$  at the same height ( $z_B = z_A = z$ ) but far† from the hole we obtain

$$\frac{\partial \phi}{\partial t} \Big|_R + \frac{\dot{R}^2}{2} = gz. \quad (4.14)$$

In this expression, we have assumed that the pressure in the air cavity is constant, equal to  $p_0$ , and that surface tension is negligible. The first assumption holds provided  $\rho_{air} U^2$  remains small compared to  $\rho g R_0$ . This constraint imposes a limit on the Froude number:  $Fr < \rho / \rho_{air} \approx 800$ . This criterion is satisfied in all the experiments presented in the present article. The second assumption on the role of surface tension holds provided  $\sigma / R_0$  is small compared to  $\rho g R_0$ . This implies that the geometrical length

† Far means that  $B$  is chosen ‘far enough’ from the hole so that no motion is observed at  $B$ : both the velocity and the acceleration are small compared to the velocity and acceleration at  $A$ .

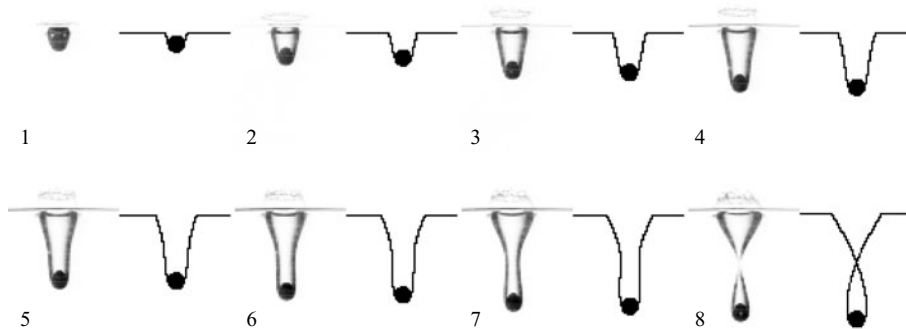


FIGURE 13. Comparison between the cavity observed experimentally with a solid sphere of radius  $R = 11.5$  mm and Froude number  $Fr = 52$  (left-hand image) and the numerical integration of equation (4.18) (right-hand image).

$R_0$  must be chosen large compared to the capillary length  $a \equiv \sqrt{\sigma/(\rho g)}$ . The present study is conducted in this limit  $R_0/a \gg 1$ .

With these assumptions, the challenge now is to make an appropriate choice for the potential  $\phi$ : a direct extension of the method used to solve the Besant–Rayleigh problem consists of assuming a purely radial motion  $ru = R\dot{R}$ , which leads to

$$\phi = R\dot{R} \ln(r/R_\infty), \quad R < r < R_\infty \quad (4.15)$$

$$= 0, \quad r > R_\infty. \quad (4.16)$$

In this expression for the velocity potential,  $R_\infty$  is a function of time which can be evaluated through an assumption on the total kinetic energy: At a depth  $z$ , we consider a layer of liquid of thickness  $dz$ . The total kinetic energy in this layer is  $T \equiv \frac{1}{2} \int_R^{R_\infty} \rho 2\pi r dr dz u^2$ . Using the above evaluation of the velocity we can integrate this expression and find  $T = \pi\rho dz R^2 \dot{R}^2 \ln(R_\infty/R)$ . Since all the motion is radial, this kinetic energy comes from the motion of the liquid layer  $\pi R^2 dz$ . Assuming that  $T \approx \pi R^2 dz \dot{R}^2$ , this suggests that  $\ln(R_\infty/R) \approx 1$ , which states that the motion in the liquid extends over a region of the order of the local size of the hole  $R$  ( $R_\infty \approx 2.7 R$ ).

Using this expression for the potential, we can simplify the momentum equation (4.14) and get the equation for the cavity:

$$R\ddot{R} + \frac{3}{2}\dot{R}^2 = -gz. \quad (4.17)$$

The only difference with the equation (4.5) obtained for the Besant–Rayleigh problem is that the pressure is not constant but depends linearly on  $z$ . At a given  $z$ , this equation for the cylindrical cavity can be integrated once:

$$\dot{R}^2 = \alpha U^2 \left( \frac{R_0}{R} \right)^3 + \frac{2}{3}gz \left[ \left( \frac{R_0}{R} \right)^3 - 1 \right] \quad (4.18)$$

where we have used the limit condition  $\dot{R}^2(R = R_0) = \alpha U^2$  with  $\alpha$  a constant smaller than 1. Since  $H = Ut$  is the depth of the cavity at time  $t$ , we integrate equation (4.18) numerically from  $z = 0$  to  $z = H$  and for each  $z$  location from  $t = 0$  to  $(H - z)/U$ , using the initial condition  $R(t = 0) = R_0$ . The results obtained are compared to the experimental observations in figure 13, where the solid sphere ( $R = 11.5$  mm) impacts with a Froude number  $Fr = 52$ . The numerical integration is done with  $\alpha = 0.1$ . The comparison reveals that the general features observed experimentally are captured

by the model: the cavity slightly expand radially during the creation of the cavity, prior to a pinching which occurs roughly at mid distance between the surface and the bottom of the hole.

This comparison enables us to check the validity of the assumptions used to guess the potential.

*Approximate analytical solution for the time evolution of the shape*

We still have to integrate equation (4.18) numerically to obtain the evolution of the shape of the cavity and we do not have an analytical expression for this shape which would allow us to determine its main characteristics: when does the pinching occur? At which location? How does the depth of the cavity (at pinching) vary with the Froude number? To answer these basic questions we have developed an approximate analytical solution, the validity of which has been discussed in §4.1. The method consists of making the approximation  $R\ddot{R} + 3/2\dot{R}^2 \approx \ddot{R}^2/2$ . This reduces equation (4.17) to

$$\ddot{R}^2 \approx -2gz \quad (4.19)$$

which can be integrated twice:

$$R^2 = R_0^2 + 2\sqrt{\alpha}R_0Ut - gzt^2 \quad (4.20)$$

where we have used the initial conditions  $R(t=0) = R_0$  and  $\dot{R}(t=0) = \sqrt{\alpha}U$ . This equation (4.20) describes the time evolution of the radius of the cavity at the depth  $z$ , starting at the time when the impactor reach  $z$ . When the impactor reaches the depth  $H > z$ , the radius of the cavity at  $z$  is obtained from equation (4.20), taking  $t \equiv (H-z)/U$ . This is the case as long as the velocity is constant during the creation of the cavity. Considering the experiments presented in figures 1, 3 and 7, this assumption is reasonable. The whole shape of the cavity when the impactor reaches  $H$  is thus obtained from equation (4.20) by changing  $t$  to  $(H-z)/U$  and leads to

$$R^2 = R_0^2 + 2\sqrt{\alpha}R_0U \left( \frac{H-z}{U} \right) - gz \left( \frac{H-z}{U} \right)^2. \quad (4.21)$$

Using  $\eta \equiv H/R_0$ ,  $\epsilon \equiv 1/Fr$ ,  $\bar{z} \equiv z/H$  and  $\bar{R} \equiv R/R_0$ , the cavity shape can be written in a dimensionless form:

$$\bar{R}^2 = 1 + 2\sqrt{\alpha}\eta(1-\bar{z}) - \epsilon\eta^3\bar{z}(1-\bar{z})^2. \quad (4.22)$$

This approximate analytical solution is compared to the shape observed experimentally in figure 14. The main features of the cavity are captured by this analytical solution. We can now use this expression for the cavity shape to analyse in more detail the characteristics of the cavity.

The first question we address is the depth of the cavity at pinching. From equation (4.22), we seek  $\eta$  such that there is a  $\bar{z}$  value where  $R=0$ . This can be done by looking for the extremal locations (where  $d\bar{R}/d\bar{z}=0$ ). According to equation (4.22) there can be two such locations:

$$\bar{z}_{min} = \frac{2}{3} - \frac{1}{3}\sqrt{1 - 6\frac{\sqrt{\alpha}}{\epsilon\eta^2}} \quad \text{and} \quad \bar{z}_{max} = \frac{2}{3} + \frac{1}{3}\sqrt{1 - 6\frac{\sqrt{\alpha}}{\epsilon\eta^2}} \quad (4.23)$$

where  $\bar{z}_{min}$  and  $\bar{z}_{max}$  respectively correspond to the location of the minimum and maximum radial extent of the cavity. Since we are looking for the pinching position,

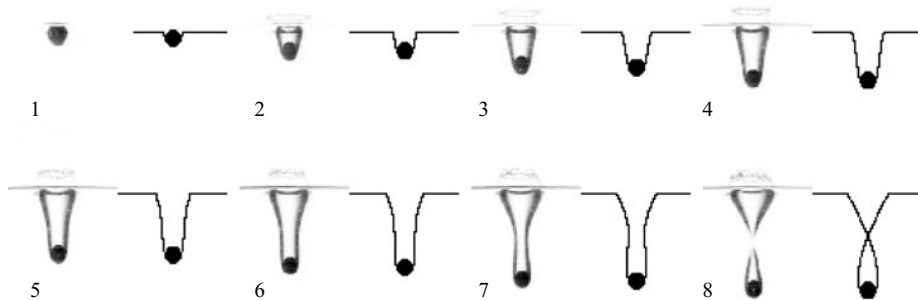


FIGURE 14. Comparison between the cavity observed experimentally with a solid sphere of radius  $R = 11.5$  mm and Froude number  $Fr = 52$  and the analytical solution (4.22).

we consider the minimum radius which can be written:

$$\bar{R}_{min}^2 = 1 + \frac{2}{9}\sqrt{\alpha}\eta \left[ 3 + 2\sqrt{1 - \frac{6\sqrt{\alpha}}{\epsilon\eta^2}} \right] - \frac{2}{27}\epsilon\eta^3 \left[ 1 + \sqrt{1 - \frac{6\sqrt{\alpha}}{\epsilon\eta^2}} \right]. \quad (4.24)$$

At pinching,  $\bar{R}_{min} = 0$  and equation (4.24) gives the relation between the depth of the cavity ( $\eta \equiv H/R_0$ ) and the Froude number ( $\epsilon \equiv 1/Fr$ ). Two limits lead to simplified results:

(i)  $\alpha = 0$

This limit corresponds to cavities created with no radial velocity. Experimentally, this limit can be achieved at the rear of long cylinders. In this limit, equation (4.24) reduces to

$$\eta = \left( \frac{27}{4} \frac{1}{\epsilon} \right)^{1/3}. \quad (4.25)$$

In this limit, the depth of the cavity thus increases as the  $1/3$  power of the Froude number, that is as  $U^{2/3}$ . From equation (4.23), we also see that the pinching occurs at  $H_p/H = 1/3$ .

These properties are consistent with the regime observed by Lohse *et al.* (2004) during the impact in soft sand.

(ii)  $\alpha \neq 0$  and  $\epsilon\eta^2 = O(1)$

When  $\alpha$  is finite, the term  $\sqrt{\alpha}\eta$  in equation (4.24) can become larger than unity since  $\eta \gg 1$ . At the singularity ( $\bar{R}_{min} = 0$ ), the term in  $\epsilon\eta^3$  must compensate the term of order  $\sqrt{\alpha}\eta$  and we deduce that  $\epsilon\eta^2 = O(1)$ .

In this limit, the pinching  $\bar{R}_{min} = 0$  is achieved when the last two terms on the right-hand side of equation (4.24) are equal to each other. This is achieved for

$$\eta = \left( \frac{8\sqrt{\alpha}}{\epsilon} \right)^{1/2}. \quad (4.26)$$

In this limit, the depth of the cavity increases as the square root of the Froude number, that is linearly with the velocity. From equation (4.23), we also find that the pinching location is  $H_p/H = 1/2$ .

These properties are consistent with the experimental results obtained by Glasheen & McMahon (1996a). A closer comparison is given below.

The characteristics of the cavity at pinching are summarized on figure 15 for the two different regimes identified. The transition between the two regimes is expected

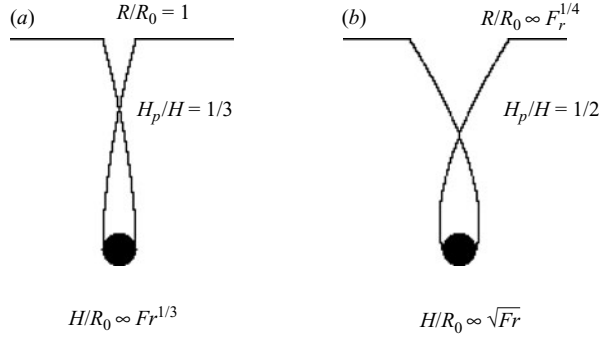


FIGURE 15. Characteristics of the cavities at the pinching for the two limits (a)  $\alpha = 0$  and (b)  $\alpha \neq 0$  and  $\epsilon\eta^2 = O(1)$ .

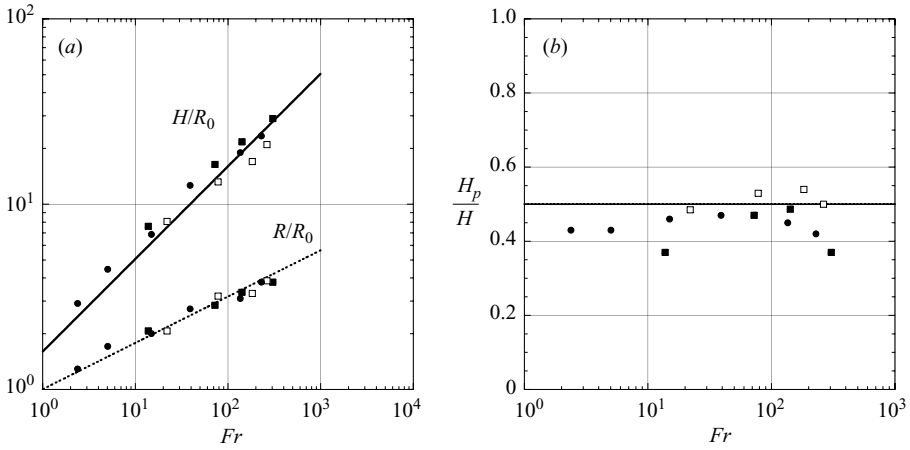


FIGURE 16. Characteristics of the cavities created by spheres: (a) Evolution of the reduced depth  $H/R_0$  and reduced crater size  $R/R_0$  as a function of the Froude number for different sphere size:  $\blacksquare$ ,  $R_0 = 6$  mm;  $\square$ ,  $R_0 = 7.8$  mm;  $\bullet$ ,  $R_0 = 12$  mm. The solid line is the law  $H/R_0 = \sqrt{(8\sqrt{\alpha})Fr}$ , plotted for  $\alpha = 0.1$ . The dashed line is the law  $R/R_0 = 2^{5/4}\alpha^{3/8}Fr^{1/4}$ , plotted with  $\alpha = 0.1$ . (b) Evolution of the reduced neck location  $H_p/H$  as a function of the Froude number for different sphere sizes as in (a). The solid line is the law  $H_p/H = 1/2$ .

when the second term on the right-hand side of equation (4.24) becomes larger than 1. This condition implies that the first regime ( $\alpha = 0$ ) can only be observed if  $\alpha \ll 0.3\epsilon^{2/3}$ .

## 5. Comparison between theory and experiments

Experimentally, we have tried to access both regimes using cylinders and spheres; as shown on figure 5(b) the impact of spheres is characterized by  $\alpha > 0$ , whereas the cavity created behind cylinders (figure 9) can be characterized by  $\alpha \approx 0$ .

### 5.1. Characteristics of the cavity at pinching

We first consider the cavities created by the impact of spheres. The measured reduced depth of the cavity ( $H/R_0$ ) obtained with different spheres is presented in figure 16(a) as a function of the Froude number. This reduced depth increases as  $Fr^{1/2}$  as predicted by equation (4.26). More quantitatively, this equation is plotted as a solid line for the value  $\alpha = 0.1$ . This theoretical evaluation of the cavity depth is in reasonable



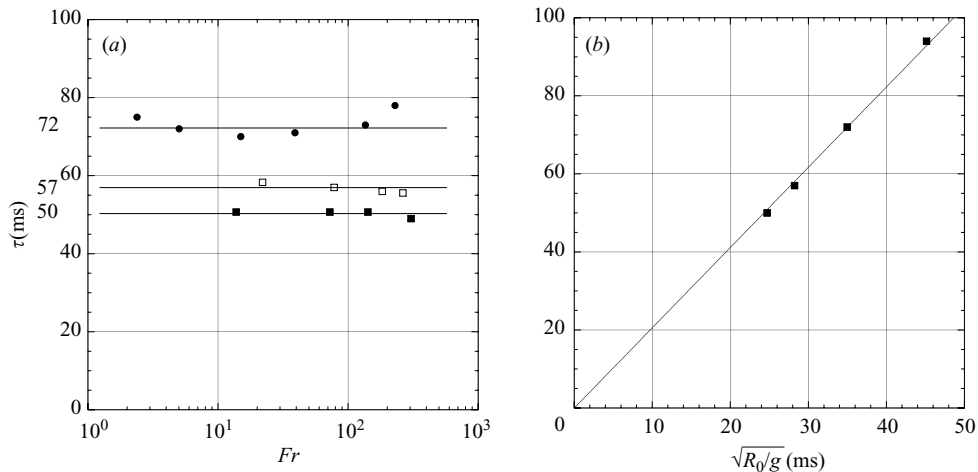


FIGURE 17. Characteristics of the cavities created by spheres: (a) Evolution of the time at pinching  $\tau$  (ms) as a function of the Froude number for different sphere size:  $\blacksquare$ ,  $R_0 = 6$  mm;  $\square$ ,  $R_0 = 7.8$  mm;  $\bullet$ ,  $R_0 = 12$  mm. The solid lines are to guide the eye. (b) Evolution of the time at pinching  $\tau$  (ms) as a function of the time  $\sqrt{R_0/g}$ . The solid line is the best fit  $\tau = 2.06\sqrt{R_0/g}$ .

agreement with our experimental data. With  $\alpha = 0.1$  the theoretical law (4.26) is  $H/R_0 = \sqrt{(8\sqrt{\alpha})Fr} \approx 1.6\sqrt{Fr}$ , which is close to the one obtained experimentally by Glasheen & McMahon (1996a) for impacting disks (radius  $R$ ):  $H/R \approx 2.297\sqrt{Fr}$ . The scaling in Froude number is the same and the prefactor is larger, which suggest that the value of  $\alpha$  depends on the geometry of the solid body.

The measured reduced crater size ( $R/R_0$ ) is also presented in figure 16(a) and shows a  $Fr^{1/4}$  dependence. The law derived in the limit  $\alpha \neq 0$  and  $\epsilon\eta^2 = O(1)$  is  $R/R_0 \approx 2^{5/4}\alpha^{3/8}Fr^{1/4}$ . It is plotted as a dashed line and is in good agreement with our experimental data.

The reduced neck position  $H_p/H$  is presented in figure 16(b) as a function of the Froude number. The dispersion of the data is important but we notice no systematic variation of the reduced neck position with the Froude number but rather a constant value close to 0.45, which is not far from the value 1/2 predicted by the theory.

The results obtained with spheres for the time  $\tau$  at pinching are presented in figure 17. In figure 17(a) we recover the observation made from figure 7 that the time at pinching  $\tau$  does not depend on the Froude number. Here, we notice that  $\tau$  increases with the radius of the sphere. This evolution can be understood from the theoretical results obtained in the limit  $\alpha \neq 0$  and  $\epsilon\eta^2 = O(1)$  and summarized in figure 15(b). If  $H/R_0 \sim Fr^{1/2}$ , the time at pinching,  $\tau \sim H/U$ , is independent of the velocity and depends linearly on  $\sqrt{R_0/g}$ . The relation  $\tau(\sqrt{R_0/g})$  is presented in figure 17(b). The linearity is achieved and the best fit reveals that  $\tau \approx 2.06\sqrt{R_0/g}$ . This value of 2.06 is higher than the one predicted by the theory for  $\alpha = 0.1$  ( $\tau = 1.6\sqrt{R_0/g}$ ). The discrepancy probably originates in the fact that the sphere does not have an exactly constant velocity as assumed by the above theoretical model.

Comparing with the experimental results of Glasheen & McMahon (1996a) obtained with an impacting disk (radius  $R$ )  $\tau \approx 2.285\sqrt{R/g}$  we observe that the law is similar with a slight difference in the prefactor, which again suggest that the prefactor depends on the parameter  $\alpha$ , the value of which depends on the geometry.

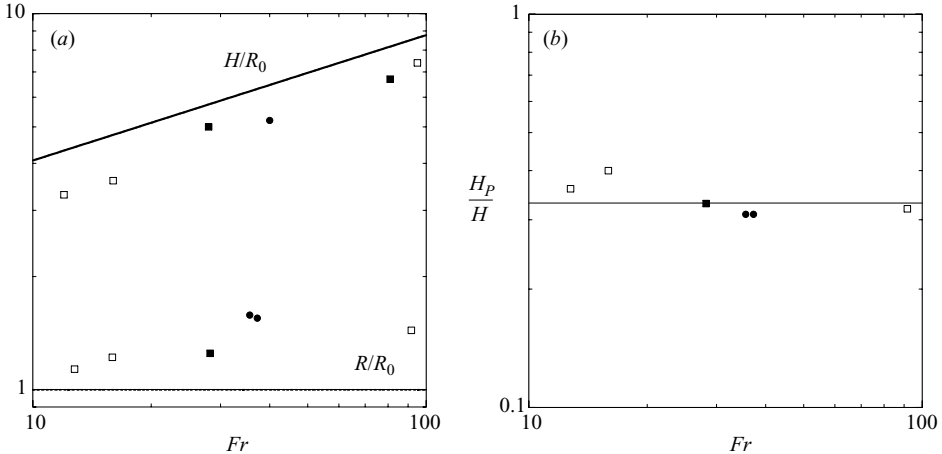


FIGURE 18. Characteristics of the cavities created by cylinders: (a) Evolution of the reduced depth  $H/R_0$  and reduced crater size  $R/R_0$  as a function of the Froude number for different cylinder size:  $\blacksquare$ ,  $R_0 = 6.1$  mm;  $\square$ ,  $R_0 = 10.1$  mm;  $\bullet$ ,  $R_0 = 20.1$  mm. The solid line is the law  $H/R_0 = (27/4 Fr)^{1/3}$  derived theoretically in the limit  $\alpha = 0$ . The dashed line is the law  $R/R_0 = 1$ . (b) Evolution of the reduced neck location  $H_p/H$  as a function of the Froude number for different: cylinder sizes as in (a). The solid line is the law  $H_p/H = 1/3$  derived in the limit  $\alpha = 0$ .

The characteristics of the cavities created by cylinders are presented in figure 18: the reduced depth  $H/R_0$  is plotted in figure 18(a) as a function of the Froude number. The solid line represents the law  $H/R_0 = (27/4 Fr)^{1/3}$  derived theoretically (equation (4.25)). It is 25% above the experimental values but seems to capture the evolution in Froude number.

The reduced crater size  $R/R_0$  is also presented on figure 18(a). No clear dependence on Froude number is observed, the data being scattered around a mean value of 1.3. This is above the theoretically expected value of  $R/R_0 = 1$  but does not contradict the prediction of no dependence on Froude number with a value close to the body size.

Finally, the reduced neck position  $H_p/H$  is presented on figure 18(b) as a function of the Froude number. Unlike the cavities created by spheres where  $H_p/H \approx 0.5$ , we observe here that the neck location is closer to the value  $H_p/H \approx 0.35$ , which is not far from the theoretical prediction  $H_p/H = 1/3$ .

## 6. Conclusion

We report the study of transient cavities created by the impact of a solid body in water at high Reynolds and high Weber numbers. In this limit, we show theoretically that an approximate analytical solution can be derived to describe the evolution in time of the cavity, from its creation to pinching.

This approximate analytical solution predicts the existence of two very different cavity dynamics, one being characterized by a reduced depth evolution  $H/R_0 \sim Fr^{1/2}$  and the other by the evolution  $H/R_0 \sim Fr^{1/3}$ . The reduced crater size is also different, one predicting  $R/R_0 \sim Fr^{1/4}$ , and the other  $R/R_0 \sim 1$ .

Experimentally, we have found both solutions, using spheres for the first regime and cylinders for the second. This geometrical parameter enables the limit condition at the contact between the solid body and the liquid, to be changed which controls

the nature of the cavity dynamics. The characteristics of the experimental cavities are in fair agreement with those expected from the theory.

## REFERENCES

- BACHELOR, G. K. 1967 *An Introduction to Fluid Dynamics*. Cambridge University Press.
- BESANT, W. H. 1859 *Hydrostatics and Hydrodynamics*. Cambridge University Press.
- BIRKHOFF, G. & ZARANTONELLO, E. H. 1957 *Jets, Wakes and Cavities*. Academic.
- BRENNEN, C. E. 1995 *Cavitation and Bubble Dynamics*. Oxford University Press.
- BRENNER, M. P., HILGENFELDT, S. & LOHSE, D. 2002 Single bubble sonoluminescence. *Rev. Mod. Phys.* **74**, 425.
- CHANDRASEKHAR, S. 1981 *Hydrodynamic and Hydromagnetic Stability*. Dover.
- COINTEM, R. 1989 Two-dimensional water-solid impact. *J. Offshore Mech. Arctic Engng* **111**.
- DUEZ, C., YBERT, C., CLANET, C. & BOCQUET, L. 2007 Making a splash with water repellency. *Nature* **3**, 180–183.
- EGGERS, J. 2007 News and views: Coupling the large and the small. *Nature* **3**, 145–146.
- FRIDMAN, G. M. 1998 Matched asymptotics for two-dimensional planing hydrofoils with spoilers. *J. Fluid Mech.* **358**, 259–281.
- DE GENNES, P. G., BROCHARD, F. & QUÉRÉ, D. 2004 *Capillary and Wetting Phenomena: Drops, Bubbles, Pearls, Waves*. Springer.
- GLASHEEN, J. W. & MCMAHON, T. A. 1996a Vertical water entry of disks at low Froude numbers. *Phys. Fluids* **8**, 2078–2083.
- GLASHEEN, J. W. & MCMAHON, T. A. 1996b A hydrodynamic model of locomotion in the basilisk lizard. *Nature*, **380** 340–342.
- HILGENFELDT, S., BRENNER, M. P., GROSSMANN, S. & LOHSE, D. 1998 Analysis of Rayleigh-Plesset dynamics for sonoluminescing bubbles. *J. Fluid Mech.* **365**, 171–204.
- HOWISON, S. D., OCKENDON, J. R. & WILSON, S. K. 1991 Incompressible water-entry problems at small deadrise angle. *J. Fluid Mech.* **222**, 215–230.
- VON KÁRMÁN, T. 1929 The impact on seaplane floats during landing. *NACA TN* 321.
- KOROBKIN, A. A. & PUKHNACHOV, V. V. 1988 Initial stages of water impact. *Annu. Rev. Fluid Mech.* **20**, 159–185.
- LOHSE, D., BERGMANN, R., MIKKELSEN, R., ZEILSTRA, C., VAN DER MEER, D., VERSLUIS, M., VAN DER WEELE, K., VAN DER HOEF, M. & KUIPERS, H. 2001 Impact on soft sand: void collapse and jet formation. *Phys. Rev. Lett.* **93**, 198003.
- MAY, A. 1952 Vertical entry of missiles into water. *J. Appl. Phys.* **23**, 1362–1372.
- OLIVER, J. M. 2002 Water entry and related problems. PhD/DPhil thesis, University of Oxford.
- RAYLEIGH, LORD 1892 On the instability of cylindrical fluid surfaces. *Phil. Mag.* **34**, 177–180.
- RAYLEIGH, LORD 1917 On the pressure developed in a liquid during the collapse of a spherical cavity. *Phil. Mag.* **XXXIV**, 94–98.
- RICHARDSON, E. G. 1948 The impact of a solid on a liquid surface. *Proc. Phys. Soc.* **61**, 352–367.
- THORODDSEN, S. T. & SHEN, A. Q. 2001 Granular jets. *Phys. Fluids* **13**, 4–6.
- WAGNER, H. 1932 Phenomena associated with impacts and sliding on liquid surfaces. *Z. Angew. Math. Mech.* **12**, 193–235.
- WORTHINGTON, A. M. 1908 *A Study of Splashes*. Longmans Green and Company.
- WORTHINGTON, A. M. & COLE, R. S. 1900 Impact with a liquid surface studied by the aid of instantaneous photography. Paper II. *Phil. Trans. R. Soc. Lond. A* **194**, 175–199.